PAPER

Check for updates

SnO–Sn₃O₄ heterostructural gas sensor with high response and selectivity to parts-per-billion-level NO₂ at low operating temperature†

Wenwen Zeng, [ID] [a] Yingzhi Liu,[a] Guoliang Chen,[a] Haoran Zhan,*[a] Jun Mei,*[a] Nan Luo,[a] Zhoukun He [ID] [b] and Changyu Tang [ID] [a]

Considering the harmfulness of nitrogen dioxide (NO₂), it is important to develop NO₂ sensors with high responses and low limits of detection. In this study, we synthesize a novel SnO–Sn₃O₄ heterostructure through a one-step solvothermal method, which is used for the first time as an NO₂ sensor. The material exhibits three-dimensional flower-like microparticles assembled by two-dimensional nanosheets, *in situ*-formed SnO–Sn₃O₄ heterostructures, and large specific surface area. Gas sensing measurements show that the responses of the SnO–Sn₃O₄ heterostructure to 500 ppb NO₂ are as high as 657.4 and 63.4 while its limits of detection are as low as 2.5 and 10 parts per billion at 75 °C and ambient temperature, respectively. In addition, the SnO–Sn₃O₄ heterostructure has an excellent selectivity to NO₂, even if exposed to mixture gases containing interferential part with high concentration. The superior sensing properties can be attributed to the *in situ* formation of SnO–Sn₃O₄ p–n heterojunctions and large specific surface area. Therefore, the SnO–Sn₃O₄ heterostructure having excellent NO₂ sensing performances is very promising for applications as an NO₂ sensor or alarm operated at a low operating temperature.

1. Introduction

Nitrogen dioxide (NO₂) is one of the most harmful air pollutants, which can cause the formation of acid rain, photochemical smog, and ozone in the atmosphere. It can also cause chronic bronchitis, emphysema, and respiratory irritation even at a small concentration.[1–3] The annual, daily, and hourly safe concentrations of NO₂ are approximately 21.2, 42.4, and 106.0 parts per billion (ppb), respectively, according to the Chinese ambient air quality standard (GB3095-2012). Therefore, it is important to develop NO₂ sensors with high sensitivities and low limits of detection for environment and human health protection.

Metal oxide sensors are widely used for gas sensing owing to their high sensitivities, low costs, simple fabrications, and long-term stabilities.[4] Various NO₂ sensors have been developed based on different metal oxides, such as WO₃, ZnO, In₂O₃, NiO, and SnO₂.[5–8] Among these metal oxides, SnO₂ is one of the most investigated materials owing to its excellent thermal and chemical stabilities,[9] and thus has been used for the detection of

different gases with various morphological or chemical modifications.[10–17] SnO₂ is a wide-band-gap (∼3.6 eV) n-type semiconductor with an oxidation state of +4. In addition to SnO₂, tin oxides with other oxygen stoichiometries, such as SnO, Sn₂O₃,[18] Sn₃O₄,[19] and Sn₅O₆,[20] exist. Among these tin oxides, SnO and Sn₃O₄ have also been used as gas sensing materials.[21–24] Suman compared the NO₂ sensing properties of SnO₂, SnO, and Sn₃O₄ nanobelts synthesized by carbothermal reduction. The Sn₃O₄ and SnO nanobelts exhibited better responses to NO₂ than that of SnO₂, which could be attributed to lone pairs on the surfaces of Sn₃O₄ and SnO, providing more active sites for NO₂.[9]

The formation of a p–n heterostructure is an effective method to improve the gas sensing capabilities of metal oxide gas sensors. The p–n heterostructures can adjust the electronic and chemical properties through chemical bonding and charge transfer at the interface and thus improve the gas sensing performance.[25,26] Numerous studies have been reported on improvements in gas sensing properties by the formation of p–n heterostructures including CuO–SnO₂,[27] CuO–In₂O₃,[28] CuO–ZnO,[29] Cr₂O₃–SnO₂,[30] and NiO–SnO₂.[31] Owing to the differences in semiconductor type and bandwidth of tin oxides, they can form p–n heterojunctions and increase the gas sensing performances. Li fabricated a SnO₂–SnO nanostructure with a p–n heterojunction through a simple hydrothermal process.[32] The SnO₂–SnO composite exhibited an increased sensing performance for NO₂ detection with a low limit of detection, low operating temperature (50 °C), and high sensing selectivity. Yu

ᵃChengdu Green Energy and Green Manufacturing Technology R&D Center, Chengdu Development Center of Science and Technology, China Academy of Engineering Physics, Chengdu, 610200, China. E-mail: zhanhenry20@gmail.com; meijun12@126.com

ᵇInstitute for Advanced Study, Chengdu University, Chengdu, 610106, China

† Electronic supplementary information (ESI) available. See DOI: 10.1039/d0ra05576j

fabricated a SnO–SnO$_2$ p–n heterostructure by simple hydrothermal and annealing processes.[33] The p–n heterostructural sensor exhibited excellent performances for NO$_2$ sensing at room temperature including a fast response, high sensitivity, and low limit of detection with a stable and repeatable response pattern. Shanmugasundaram synthesized SnO–SnO$_2$ composites with *in situ* p–n heterojunctions by a simple hydrothermal method.[34] The sensor response, selectivity, and sensitivity to H$_2$ were improved by the heterostructure and its optimal operating temperature was considerably lower than that of pure SnO$_2$. In these studies, the p–n heterojunctions played important roles in the sensing performance improvements. The p–n heterojunction formed at the SnO–SnO$_2$ interface narrowed the forbidden band, promoting the transition of electrons, which contributed to the enhancement in gas sensing performance. Although the SnO–SnO$_2$ p–n heterostructure had good NO$_2$ sensing performances at low temperatures, the response was not sufficiently high, which hinders its use for the detection of a low concentration of NO$_2$.

Sn$_3$O$_4$ is an n-type semiconductor with a band gap of 2.2–2.9 eV,[21] narrower than that of SnO$_2$. If Sn$_3$O$_4$ is used to replace SnO$_2$ to form a SnO–Sn$_3$O$_4$ heterostructure, the forbidden band will be further narrowed and the transition of electrons will be further enhanced, which will improve the NO$_2$ sensing performance. Furthermore, the lone pair electrons on the surface of Sn$_3$O$_4$ help the adsorption of NO$_2$ and enhance the response. Zeng used Sn$_3$O$_4$ modified hierarchical SnO$_2$, the electron injection from Sn$_3$O$_4$ to SnO$_2$ played an important role in the improvement of NO$_2$ sensing performance.[35] Therefore, the SnO–Sn$_3$O$_4$ heterostructure is likely to exhibit an outstanding NO$_2$ sensing performance.

In this study, we synthesized a novel SnO–Sn$_3$O$_4$ heterostructure through a simple one-step solvothermal method and for the first time evaluated its use as an NO$_2$ sensor. Its micromorphology, crystal structure, and chemical composition were characterized by scanning electron microscopy (SEM), transmission electron microscopy (TEM), atomic and electrostatic force microscopy (AFM and EFM), X-ray diffraction (XRD), and X-ray photoelectron spectroscopy (XPS). Furthermore, its gas sensing performances for NO$_2$ and other contrast gases were investigated. The SnO–Sn$_3$O$_4$ heterostructure exhibited excellent responses to a ppb level of NO$_2$ at its optimal operating temperature of 75 °C and ambient temperature. Moreover, the limits of detection of the SnO–Sn$_3$O$_4$ heterostructure were as low as 2.5 and 10 ppb at 75 °C and ambient temperature, respectively. In addition, the SnO–Sn$_3$O$_4$ heterostructure exhibited an excellent selectivity to NO$_2$, even if in a mixture with interferential gases in high concentration. The possible sensing mechanism is discussed. The main factors for the enhancements were attributed to the formation of p–n heterojunctions and large specific surface area of the material.

2. Experiments

2.1 Material synthesis

All chemicals used in this study were of analytical grade and used as received without further purification. Stannous chloride dihydrate (SnCl$_2$·2H$_2$O) was purchased from Aladdin Regent Co., Ltd., while urea (CO(NH$_2$)$_2$), sodium hydroxide (NaOH), and absolute ethyl alcohol (C$_2$H$_5$OH) were purchased from Kelon Chemical.

The SnO–Sn$_3$O$_4$ heterostructure was synthesized by a simple solvothermal process. In a typical synthesis procedure, 1.536 g of NaOH, 1.280 g of urea, and 0.723 g of SnCl$_2$·2H$_2$O were sequentially added to a mixture solvent consisting of 25 mL of absolute ethyl alcohol and 55 mL of deionized water under moderate stirring. After the stirring for 3 h, the solution was transferred into a 100 mL teflon-lined stainless-steel autoclave and the solvothermal process was performed at 180 °C for 18 h. The precipitates were collected and consecutively washed six times by deionized water and absolute ethyl alcohol by centrifugation (10 000 rpm). The collected product was dried at 60 °C for 10 h in a drying oven to obtain the as-prepared sample. To evaluate the influence of the composition on the sensing performance, as-prepared samples were calcined at 550 and 700 °C under ambient atmosphere for 2 h, yielding two other samples.

2.2 Characterization

The composition and crystalline structure of the sample were characterized by powder XRD using a Bruker D2 Phaser in the 2θ range of 10–80° with Cu Kα irradiation at 30 kV. XPS was performed using an ESCALA B250Xi spectrometer with a monochromatic Al excitation source. Its morphology was observed using field-emission SEM (Hitachi S5200) at an accelerating voltage of 5 kV. High-resolution (HR) morphology images and selected-area electron diffraction (SAED) patterns were acquired by using TEM (FEI Tecnai G2 F20) at an accelerating voltage of 200 kV. More detailed information of phase distribution was obtained through atomic and electrostatic force microscopy (AFM and EFM) measurements by using a MFP-3D-SA microscopy. The Brunauer–Emmett–Teller (BET) specific surface areas and pore size distributions of the samples were measured using an Autosorb-IQ2 analyzer. Ultraviolet (UV)-visible spectra were acquired using an SP-756 analyzer.

2.3 Fabrication and evaluation of the gas sensor

A spot of the prepared sample was mixed with a drop of deionized water using a mortar to form a homogeneous paste. The paste was uniformly coated on top of a gas sensor component, and then assembled into a gas sensor (Fig. S1†). The thickness of the sensing film was about 10–15 μm. Before the evaluation, the gas sensors were aged for 10 days at approximately 150 °C (heating current of 70 mA, heating resistance of 53 ± 5 Ω at ambient temperature). SnO was reported to be stable below 370 °C,[36] so the aging process would not change the phase of sensing materials. After the aging, the gas sensing performances of the sensor were evaluated using a CGS-8 intelligent gas sensing analysis system (Beijing Elite Co., Ltd., China) under laboratory conditions (approximately 25 ± 3 °C, relative humidity in the range of 50% to 60%). Static sensing test was used to evaluate the sensing performance of the sensors by injecting a certain volume of 5000 ppm standard NO$_2$ into a gas

sensor chamber whose volume was 1 L. The operating temperature of the sensor was controlled by adjusting the heating current. The measurement circuit used in the experiments is shown in Fig. S2.† The response (R) of the gas sensor was defined as the ratio of the sensor resistance in the gas (R_g) to that in the air (R_a) for oxidizing gases ($R = R_g/R_a$), such as NO_2, and inversely for reductive gases ($R = R_a/R_g$), such as volatile organic compounds (VOCs). The response and recovery times (t_{res} and t_{rec}) were defined as the times to achieve 90% of the total resistance changes in the response and recovery, respectively.

3. Results and discussion

3.1 X-ray diffraction (XRD) patterns

The compositions and crystalline structures of the samples were characterized by XRD, as shown in Fig. 1. The as-prepared sample was composed of SnO (Joint Committee on Powder Diffraction Standards (JCPDS) no. 06-0395, marked by ●) and Sn_3O_4 (JCPDS no. 16-0737, marked by ◆). The (002) and (001) peaks of SnO are the first and second highest in the pattern, respectively, showing the dominant SnO phase in the sample. Compared with the standard diffraction pattern (JCPDS no. 06-0395), the (002) and (001) peaks of SnO in the pattern of the as-prepared sample are the two highest peaks, rather than the (101) and (110) peaks. This suggests that the formed SnO phase in the as-prepared sample is predominated by exposed (002) and (001) facets. The peaks of Sn_3O_4 are observed in the range of 26–34° (bottom inset in Fig. 1), but their intensities are considerably lower than those of SnO. The XRD results show the SnO–Sn_3O_4 composition of the as-prepared sample. After the calcination at 550 °C, the peaks of SnO are vanished and replaced by those of SnO_2 (JCPDS no. 41-1445, marked by ■). This transition in the XRD pattern demonstrates the decomposition and oxidization of SnO into SnO_2.[19,37] Although the Sn_3O_4 peaks are decreased, they can still be distinguished, as shown in the top inset in Fig. 1. This shows the SnO_2–Sn_3O_4
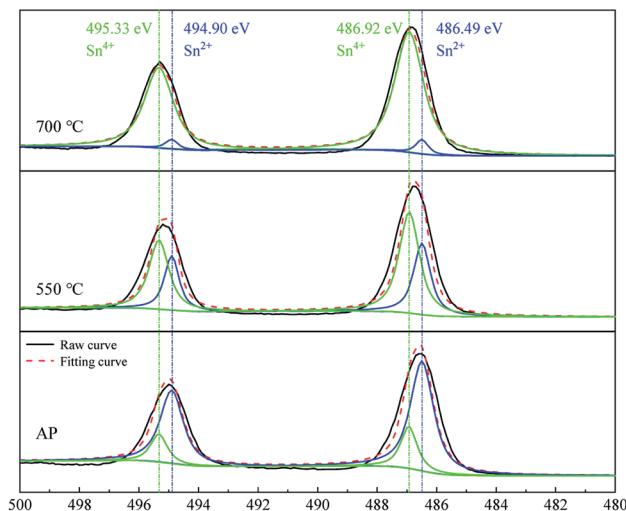

Fig. 2 HR Sn 3d X-ray photo electron spectrum of the samples.

composition of the sample calcined at 550 °C. After the calcination at 700 °C, only the SnO_2 peaks can be distinguished in the XRD pattern, showing that SnO and Sn_3O_4 entirely decomposed and oxidized into SnO_2.

3.2 X-ray photoelectron spectroscopy (XPS)

The chemical compositions and oxidation states of the samples were further characterized by XPS. Fig. S3† presents a full-scan X-ray photo electron spectrum of the as-prepared sample, showing the characteristic peaks of Sn, O, and C without other impurities. To understand the valence states of the tin element, the HR Sn 3d spectrum was analyzed, as shown in Fig. 2. The deconvolution of the spectrum yielded four Gaussian peaks. The fitted peaks at 495.33 and 486.92 eV correspond to the Sn^{4+} state, while those at 494.90 and 486.49 eV correspond to the Sn^{2+} state. For the as-prepared sample, the peak area of Sn^{2+} is larger than that of Sn^{4+}, which demonstrates the domination of Sn^{2+} state. This is consistent with the XRD results, further confirming the phase composition of major SnO and minor Sn_3O_4. The ratio of the peak areas between Sn^{2+} and Sn^{4+} is 3.67, and the calculated mole ratio of SnO to Sn_3O_4 is 1.67 (a Sn_3O_4 unit cell contain two Sn^{2+} and one Sn^{4+} atoms[38]). After the calcination at 550 °C, the peaks are shifted to higher binding energies and those of Sn^{4+} are dominant. After the calcination at 700 °C, the peaks are further shifted to higher binding energies, which well match with the binding energies of Sn^{4+}, while the peaks of Sn^{2+} are almost vanished. The XPS results of the Sn-related states obtained in this experiment demonstrate the transition of Sn^{2+} to Sn^{4+} during the calcination, consistent with the XRD results.

3.3 Morphological evaluation

The morphologies of the samples were characterized by field-emission SEM, as shown in Fig. 3. Fig. 3(a) and (b) show field-emission SEM images of the as-prepared sample. The material is composed of microparticles with diameters of 2 to 4 μm. The
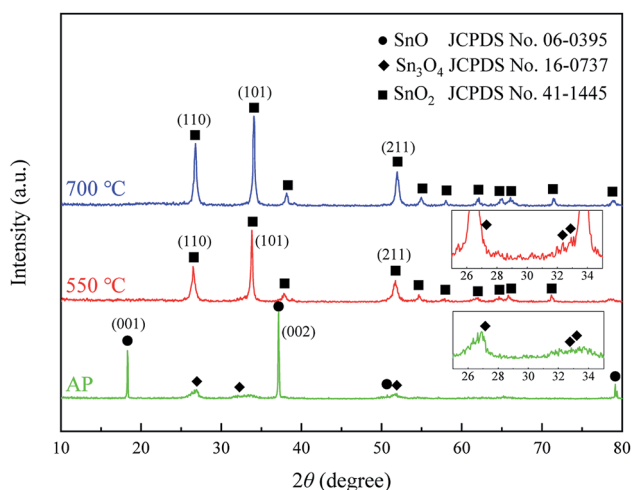

Fig. 1 XRD patterns of the as-prepared sample (denoted as AP) and samples calcined at 550 and 700 °C.
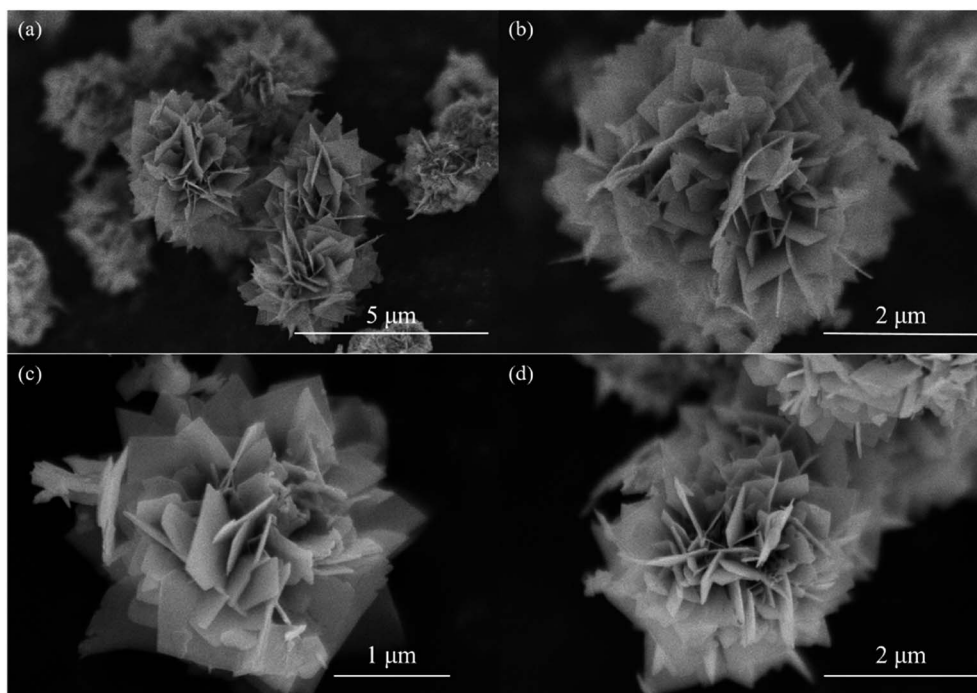
Fig. 3 SEM images of (a) and (b) as-prepared sample; (c) sample calcined at 550 °C; (d) sample calcined at 700 °C.

microparticles consist of large numbers of two-dimensional nanosheets and have flower-like morphologies. The microparticles exhibit a two–three-dimensional (2–3D) hierarchical structure (*i.e.*, the 2D nanosheets are assembled into 3D microparticles).[39] After the calcinations at 550 and 700 °C, the morphologies maintain the 2–3D hierarchical structure and are similar with that of the sample obtained without calcination. This implies that the calcination has no considerable effect on the morphology.

TEM and HRTEM images and SAED pattern were acquired to investigate the microstructure of the as-prepared sample, as shown in Fig. 4. In Fig. 4(a), the peripheral nanosheets can be distinguished; the thicknesses of the nanosheets are approximately 30 nm. The HRTEM image and SAED pattern in Fig. 4(b) show further structural information about the microparticles. In the HRTEM image, the lattice fringes with interplanar crystal spacings of 0.3652 and 0.3297 nm correspond to the (101) and (111) planes of the Sn_3O_4 structure (JCPDS no. 16-0737), respectively. Lattice fringes with an interplanar crystal spacing of 0.2689 nm corresponding to the (110) planes of the tetragonal SnO structure (JCPDS no. 06-0395) are also observed. These two different phases exist at one nanosheet together, and contact with each other, form heterojunctions on the nanosheets *in situ*. Therefore, the as-prepared sample exhibited a $SnO–Sn_3O_4$
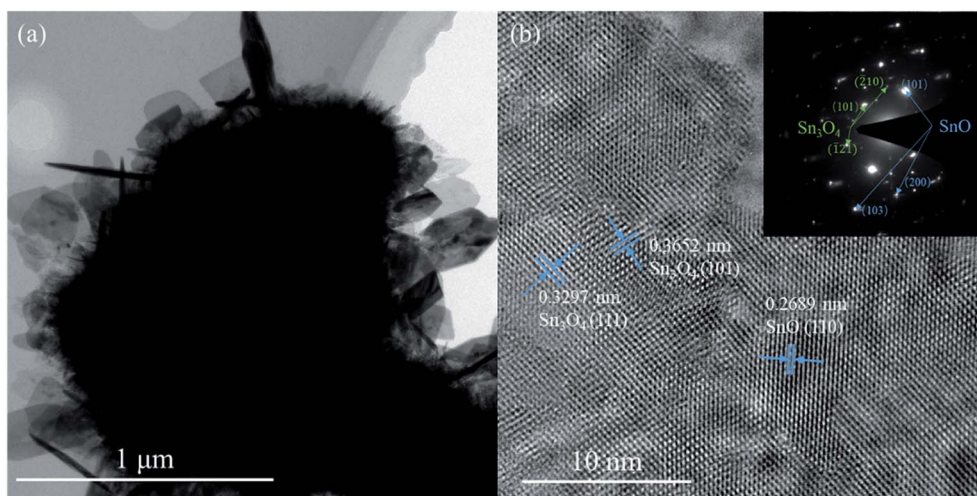

Fig. 4 (a) TEM and (b) HRTEM images and SAED pattern of the as-prepared sample.

heterostructure. The inset in Fig. 4(b) shows a SAED pattern of the as-prepared sample. SnO and Sn_3O_4 crystalline phases could be distinguished, confirming the $SnO-Sn_3O_4$ heterostructure of the material.

AFM measurement and EFM measurement with a bias voltage of 10 V were carried out to distinguish the different phases on the nanosheet more intuitively, the results are shown in Fig. 5. Before the measurement, the $SnO-Sn_3O_4$ composite was grinded and dispersed on ITO glass. It can be found that the ITO substrate is mostly white in EFM image (Fig. 5(b)) by comparing with corresponding AFM image (Fig. 5(a)), illustrating its electroconductibility. Whereas, the image of the nanosheet in Fig. 5(b) exhibits mostly black with a small part of white. This phenomenon is much more clear in the comparison of Fig. 5(c) and (d), and the white part in Fig. 5(d) correspond well to the projecting part in Fig. 5(c). This means the nanosheet contains major insulating phase and minor conductive phase. Considering the high resistance of SnO[40,41] and the phase ratio indicated by XRD, the black and white part in EFM image may well be SnO and Sn_3O_4, respectively. This result further illustrates the distribution of SnO and Sn_3O_4 phase and the *in situ* formation of $SnO-Sn_3O_4$ heterojunctions.

3.4 Gas sensing performance

The operating temperature is an important parameter of metal oxide sensors. The responses of the samples to 500 ppb of NO_2
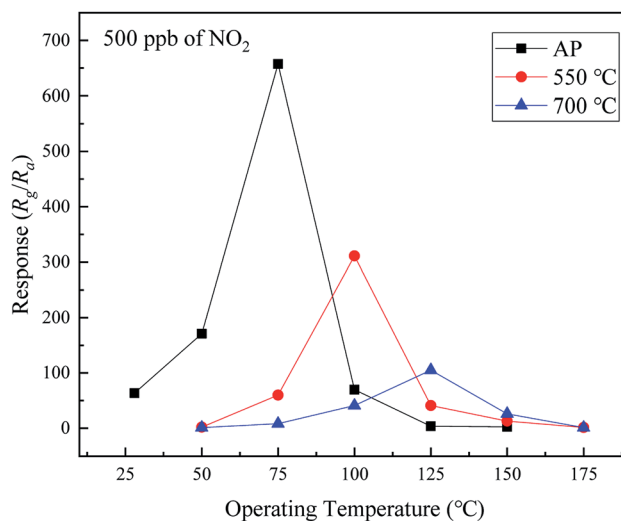

Fig. 6 Responses of the samples to 500 ppb of NO_2 as a function of the operating temperature.
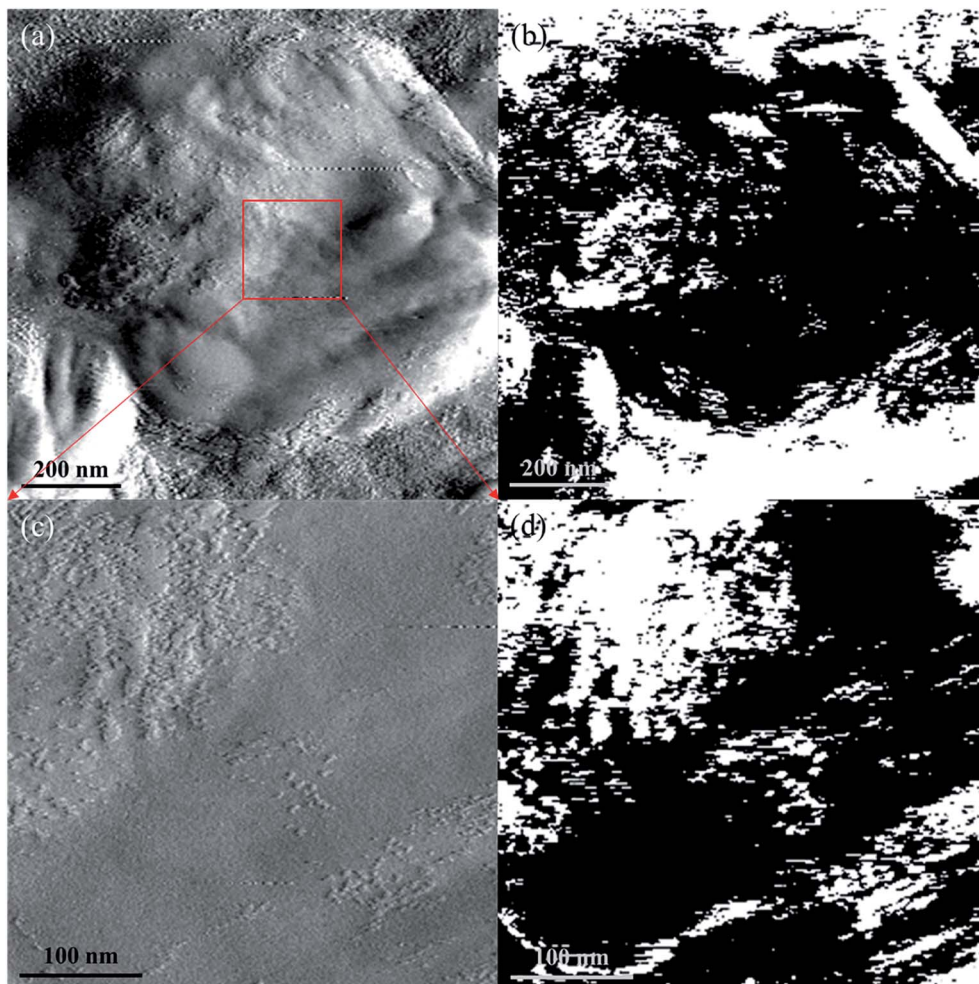

Fig. 5 AFM ((a) and (c)) and corresponding EFM ((b) and (d)) image of a nanosheet.
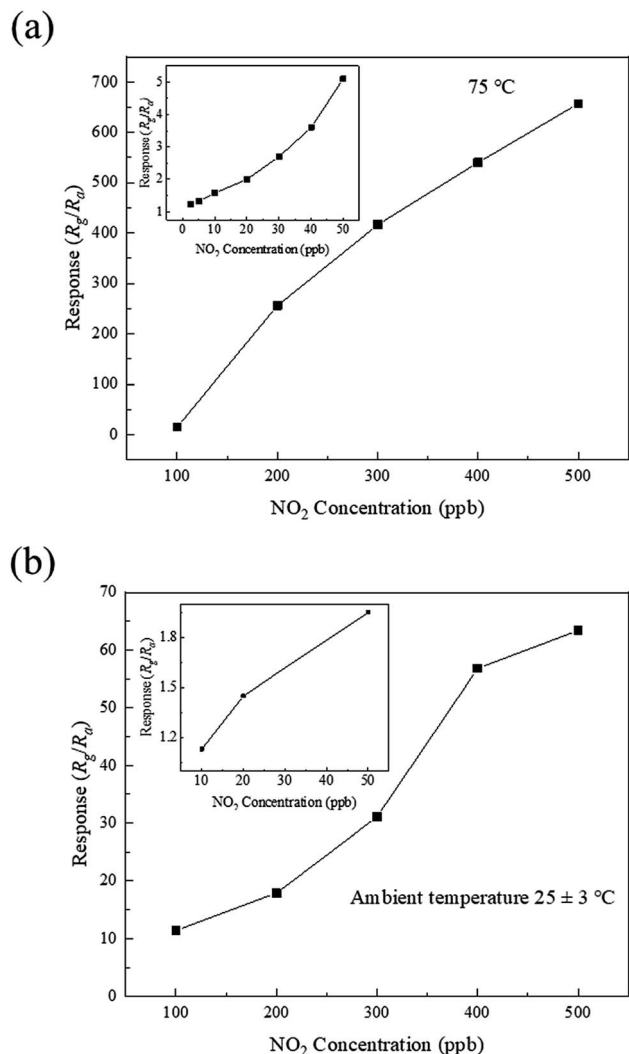
Fig. 7 Responses of the SnO–Sn$_3$O$_4$ heterostructure as a function of the NO$_2$ concentration at (a) 75 °C and (b) ambient temperature.

as a function of the operating temperature in the range of ambient temperature to 175 °C were evaluated, as shown in Fig. 6. The response of each sample increases, reaching the

maximum at a certain temperature, followed by decrease with the increase in the operating temperature. The samples exhibit different optimal operating temperatures corresponding to the highest responses (75, 100, and 125 °C for the as-prepared and 550 and 700 °C calcined samples, respectively). The highest responses of the samples are 657.4, 311.2, and 104.9, respectively. Therefore, the composition of the sample has a significant influence on its response to NO$_2$. The response of the as-prepared sample (SnO–Sn$_3$O$_4$ heterostructure) is considerably higher than those of the two other samples. It is worth noting that the SnO–Sn$_3$O$_4$ heterostructure has a response of 63.4 at ambient temperature (28 °C), which is a relatively high value.

To investigate the NO$_2$ sensing performance of the SnO–Sn$_3$O$_4$ heterostructure, the responses as a function of the NO$_2$ concentration at 75 °C and ambient temperature were evaluated, as shown in Fig. 7. As shown in Fig. 7(a), the response is high and increases with the NO$_2$ concentration (416.6, 540.1, and 657.4 at 300, 400, and 500 ppb of NO$_2$ at 75 °C, respectively). Owing to the very large resistance, the response to NO$_2$ above 500 ppb was hard to gauge. The inset in Fig. 7(a) shows the response to NO$_2$ in the range of 2.5 to 50 ppb. When the NO$_2$ concentration is as low as 2.5 ppb, the response is still 1.23, which can be easily discerned (the resistance curve of this test is shown in Fig. S4†). This implies that the detection limit of the SnO–Sn$_3$O$_4$ heterostructure is as low as 2.5 ppb, which is a relatively low concentration. These results reveal the excellent NO$_2$ sensing performance of the SnO–Sn$_3$O$_4$ heterostructure. Fig. 7(b) shows the responses at ambient temperature in the range of 50 to 500 ppb (31.1, 56.8, and 63.4 at 300, 400, and 500 ppb of NO$_2$, respectively). The response to 10 ppb of NO$_2$ at ambient temperature is 1.13, which implies that the limit of detection at ambient temperature is as low as 10 ppb. Comparison of the NO$_2$ sensing performances of the SnO–Sn$_3$O$_4$ heterostructure analyzed in this study and those in previous studies is shown in Table 1. The SnO–Sn$_3$O$_4$ heterostructure exhibits a high response and low limit of detection of NO$_2$. Therefore, the SnO–Sn$_3$O$_4$ heterostructure has an excellent NO$_2$ sensing response and very low limit of detection, not only at its optimal operating temperature of 75 °C, but also at ambient temperature. The low operating temperature is

Table 1 Comparison of the NO$_2$ sensing performance with those in previous reports

Material	Operating temperature	NO$_2$ concentration	Response	Limit of detection	Reference
SnO–SnO$_2$	RT[a]	1 ppm	4.68	0.1 ppm	33
SnO$_2$–SnO	50 °C	50 ppm	8	0.1 ppm	32
SnO$_2$–ZnO	RT UV-enhanced	1 ppm	2.4	—	42
TeO$_2$–SnO$_2$	RT	3 ppm	9.97	—	43
WS$_2$–carbon nanofibers	RT	5 ppm	20.5%	10 ppb	44
α-Fe$_2$O$_3$/rGO[b]	RT	5 ppm	8.2	50 ppb	45
In$_2$O$_3$/rGO	RT	30 ppm	8.25	—	46
Te nanotube	RT	1 ppm	30.5%	0.5 ppb	47
LaFeO$_3$ nanocube	RT	1 ppm	29.60	—	48
rGO/SnO$_2$ nanosheet	RT	100 ppm	2.87	1 ppm	49
SnO–Sn$_3$O$_4$	RT	500 ppb	63.4	10 ppb	This study
	75 °C		657.4	2.5 ppb	

[a] RT: room temperature. [b] rGO: reduced graphene oxide.

advantageous for a low energy consumption and reduced tendency for ignition, which is favorable for an increase in the service lifetime.

The resistances of the SnO–Sn$_3$O$_4$ heterostructure upon exposure to NO$_2$ in the range of 200 to 500 ppb at 75 °C and ambient temperature (28 °C) are shown in Fig. 8. The response (t_{res}) and recovery (t_{rec}) times are also shown in Fig. 8. At its optimal operating temperature, the response and recovery times of the SnO–Sn$_3$O$_4$ heterostructure decrease with the increase in the NO$_2$ concentration. At 500 ppb of NO$_2$, the response and recovery times are 178 and 87 s, respectively. At ambient temperature, the response time decreases with the increase in the NO$_2$ concentration and stabilizes around 2.5 min, which shows the quick response of the NO$_2$ sensor operated at room temperature. Nevertheless, the recovery time is much more than 20 minutes, which is a common problem for the sensors running at ambient temperature.

The selectivity is another important characteristic of metal oxide sensors. Comparison of the responses to NO$_2$ and other contrast gases is shown in Fig. 9. The responses of the contrast
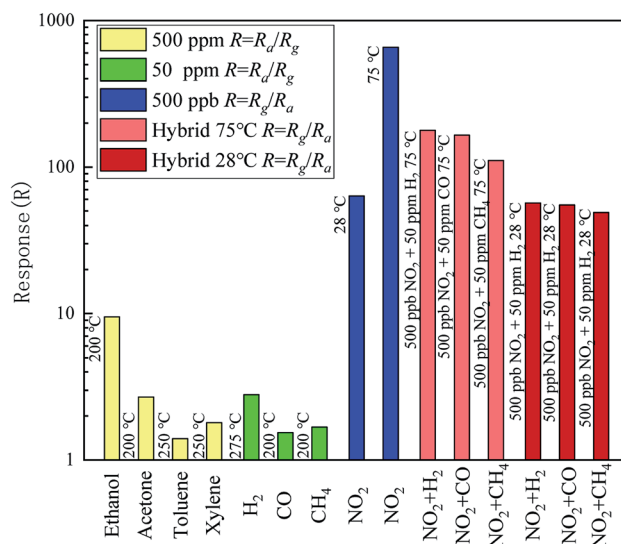

Fig. 9 Selectivity of the SnO–Sn$_3$O$_4$ heterostructure.

gases were measured at corresponding optimal operating temperatures, which are shown at the left of relevant bar. All the optimal operating temperatures of contrastive gases are not less than 200 °C, much higher than that of NO$_2$. The concentrations of the used VOCs were 500 ppm, while those of the other reductive gases (H$_2$, CO, and CH$_4$) were 50 ppm. The concentrations of all contrast gases were considerably higher than that of NO$_2$. Nevertheless, the response of the SnO–Sn$_3$O$_4$ heterostructure to NO$_2$ is hundreds or tens of times larger. What the most noteworthy is, when exposed to mixed gases consist of 500 ppb NO$_2$ and 50 ppm H$_2$, CO and CH$_4$ at 75 °C, the responses are still as high as 178.1, 165.1 and 110.9, respectively. Furthermore, when exposed to mixed gases at 28 °C, the responses of the sensor decrease just slightly compared with pure NO$_2$, illustrating that these reductive gases almost have no interference on NO$_2$ sensing at ambient temperature. These results demonstrate the excellent selectivity of the SnO–Sn$_3$O$_4$ heterostructure to NO$_2$, even if exposed to mixture gases containing interferential part in high concentration.

The short-term and long-term stability of the SnO–Sn$_3$O$_4$ heterostructure were also been tested, as shown in Fig. 10. Fig. 10(a) and (b) illustrate the resistance curve of the sensor by repetitive exposing to 100 ppb of NO$_2$ five times at 75 and 25 °C, respectively. It is clearly that all of the five resistance tracks in both figures are similar and have almost the same peak value, revealing the good reversibility of the sensor. The continuous measurement of the response of the SnO–Sn$_3$O$_4$ heterostructure to 500 ppb of NO$_2$ at 75 °C and ambient temperature for about 30 days were investigated and the results are shown in Fig. 10(c). Both of the deviations of the responses at two different work temperature are less than 5%, exhibiting good long-term stability. These experiments demonstrate the SnO–Sn$_3$O$_4$ heterostructure possesses good repeatability and stability.

This systematic analysis demonstrates the excellent NO$_2$ sensing performances of the SnO–Sn$_3$O$_4$ heterostructure including very high response, low limits of detection, and excellent selectivity to a ppb level of NO$_2$ at 75 °C and ambient
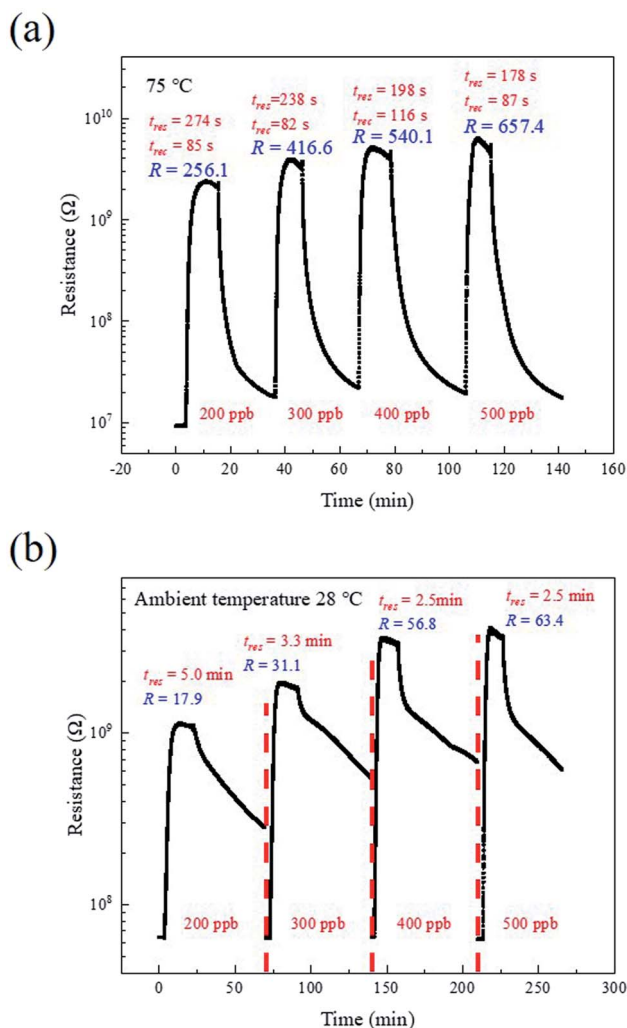

Fig. 8 Actual resistance curves of the SnO–Sn$_3$O$_4$ heterostructure at (a) 75 °C and (b) ambient temperature (28 °C).
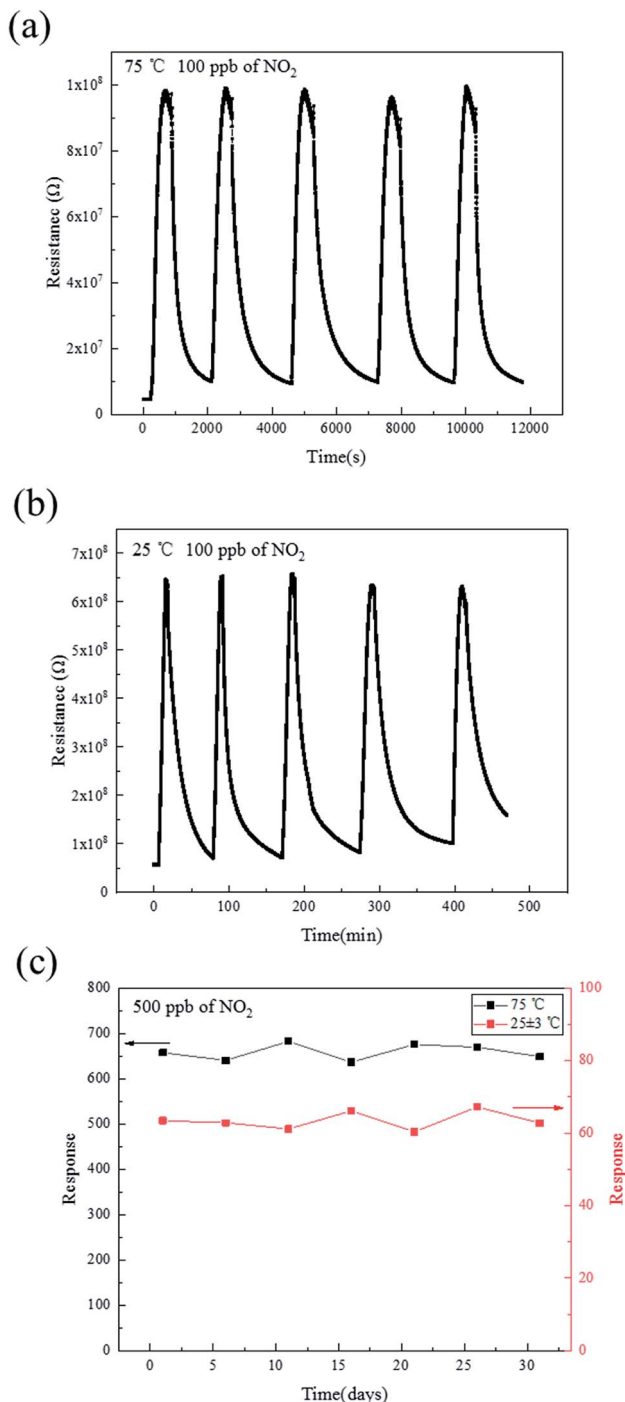
Fig. 10 Repeatability curve of SnO–Sn$_3$O$_4$ heterostructure at (a) 75 °C and (b) 25 °C; (c) long-term stability of SnO–Sn$_3$O$_4$ heterostructure at 75 °C and ambient temperature.

temperature. Therefore, the SnO–Sn$_3$O$_4$ heterostructure is very promising as an NO$_2$ sensor or alarm operated at a low or ambient temperature.

3.5 Sensing mechanism

The gas sensing mechanism of SnO–Sn$_3$O$_4$ heterostructure can be explained by common adsorption–oxidation–desorption pathway. When the SnO–Sn$_3$O$_4$ heterostructure is exposed to

clean air, O$_2$ molecules adsorb on the surface by extracting electrons from the conduction band and form oxygen anions (mainly O$_2^-$ at a low temperature[50]), yielding an electron depletion layer on the surface. The width of the depletion layer does not change after the adsorption of O$_2$ is saturated.[51] Once the sensor is exposed to NO$_2$ gas, NO$_2$ molecules adsorb on the surface by extracting electrons from the conduction bands or interacting with the chemisorbed oxygen on the surface.[33,52] To figure out the truly reactions, FTIR was used to distinguish the adsorbate on SnO–Sn$_3$O$_4$ heterostructure after the reaction of adsorbing NO$_2$, the results are shown in Fig. 11.

This figure shows the FTIR spectra of SnO–Sn$_3$O$_4$ in air and atmosphere of 1% NO$_2$ at room temperature. Both of these two curve have band at 1630 and 3421 cm^{-1}, which can be assigned to H$_2$O in the sample. Also both of them have four peaks at 481, 532, 582 and 634 cm^{-1}, which can be ascribed to Sn–O vibration.[53,54] After adsorption in 1% NO$_2$, a peak around 1384 cm^{-1} appears, which can be assigned to adsorbed NO$_2$.[55] According to previous research,[56] this peak is most likely to be NO$_3^-$. So the product of NO$_2$ adsorption on SnO–Sn$_3$O$_4$ at room temperature should be NO$_3^-$ here. The reaction equation should be[45,57]

$$2NO_2 \ (gas) + O_2^- \ (ads) + e^- \rightarrow 2NO_3^- \ (ads) \tag{1}$$
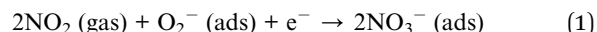
This result proves that the product of NO$_2$ adsorbing, at least at room temperature, is NO$_3^-$. This reaction consumes large numbers of electrons and increase the thickness of the depletion layer, thus increasing the potential barrier together with the sensor resistance. When the sensor is exposed to clean air again, NO$_2$ molecules desorb from the surface and release the captured electrons back to the material, leading to the recovery of the sensor resistance.

The SnO–Sn$_3$O$_4$ heterostructure exhibited a very high response at relatively low operating temperature, which might be attributed to the following factors. Firstly, the formation of p–n heterojunctions at the SnO and Sn$_3$O$_4$ interfaces could be
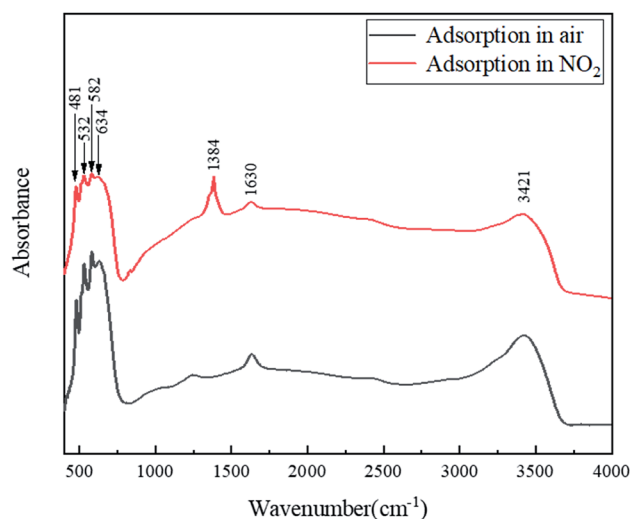

Fig. 11 FTIR spectrum of SnO–Sn$_3$O$_4$ heterostructure after adsorption in air and NO$_2$.

the primary factor contributing to the high response and low operating temperature. A plot of $(\alpha h\nu)^{1/2}$ against the photon energy ($h\nu$) for the SnO–Sn_3O_4 heterostructure and its energy structure schematic diagram are shown in Fig. 12(a) and (b), respectively. The formation of the heterojunction leads to bending of the forbidden bands to equilibrate the Fermi level (E_F) between the SnO and Sn_3O_4 band gaps, the electrons will transfer from n-type Sn_3O_4 to p-type SnO according to their work functions (5.1 eV for SnO[58] and 3.9 eV for Sn_3O_4 (ref. 59)), as shown in Fig. 12(b). Generally, a narrower forbidden band implies a lower energy required for the transition of electrons.[32] Compared with SnO_2 (typically 3.6 eV) in SnO–SnO_2 (ref. 32 and 33) composite, Sn_3O_4 in (2.12 eV in this study) SnO–Sn_3O_4 heterostructure exhibited a considerably smaller band width. Therefore, the electrons could easily transfer from the forbidden band to the conduction band at a low operating temperature and participate in the gas sensing reaction. The *in situ* formation of the SnO–Sn_3O_4 heterojunctions is conducive to increase the interfacial area and further enhance the effect of the heterojunctions. Furthermore, the formation of SnO–Sn_3O_4 heterojunctions lead to the transfer of electrons from n-type Sn_3O_4 to p-type SnO, and generate depletion layer at the interface of two phases. This depletion layer will coexist with the depletion layer formed by the adsorption of gases (O_2 and NO_2 here), and change simultaneously with the other one when the adsorbed state changes. This process facilitates the detection of NO_2 through the change in the electrical conductivity of the material.[45,60]

Secondly, the morphology of the material contributes to the performance enhancement. The N_2 adsorption–desorption isotherm of the SnO–Sn_3O_4 heterostructure and corresponding pore size distribution are shown in Fig. S5.† The calculated BET surface area of the sample is 43.86 m^2 g^{-1}, while the average pore diameter is 32.31 nm. The mesoporous structure and large specific surface area enhance the diffusion and absorption of

NO_2 molecules on the surface, thus improving the sensing performance.

The excellent selectivity of SnO–Sn_3O_4 heterostructure to NO_2 can be attributed to the reasons as follows. As discussed above, the formation of p–n heterojunctions and the large specific surface area make SnO–Sn_3O_4 heterostructure exhibit high response to NO_2 at low operating temperature. When the operating temperature increase beyond 75 °C, its response to NO_2 decrease because of the desorption of NO_2 molecules induced by high temperature. But for reductive gases (such as H_2 and ethanol), their main sensing mechanism on metal oxide sensors are reacting with adsorbed oxygen ions, for example,

$$H_2 + O^- \rightarrow H_2O + e^- \tag{2}$$

$$C_2H_5OH + 6O^- \rightarrow 2CO_2 + 3H_2O + 6e^- \tag{3}$$
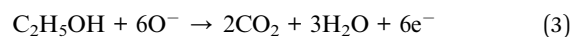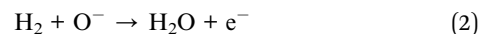
These reactions will return the electrons to the material and lead to the reduction of resistance, which is an opposite change compared with oxidizing gases. In these reactions, high temperature (higher than 200 °C in general, also this is the reason why "O^-" instead of "O_2^-" appears in eqn (2) and (3)) is a requirement. Nevertheless, the number of adsorbed oxygen anions on SnO–Sn_3O_4 heterostructure are significant reduced because of the desorption induced by high temperature when the operating temperature exceeding 75 °C. So the sensing reactions between reductive gases and oxygen anions are inactive, leading to the low response to reductive gases. When SnO–Sn_3O_4 heterostructure is exposed to mixed gases of NO_2 and reductive gases at 75 °C, although the concentrations of reductive gases are much higher, they can barely react with NO_2 molecules at this temperature, only the high concentration influences the adsorption of NO_2 molecules. Therefore, the resistances of the sensors still increase and the responses are still high when exposed to mixed gases, exhibiting excellent selectivity to NO_2.
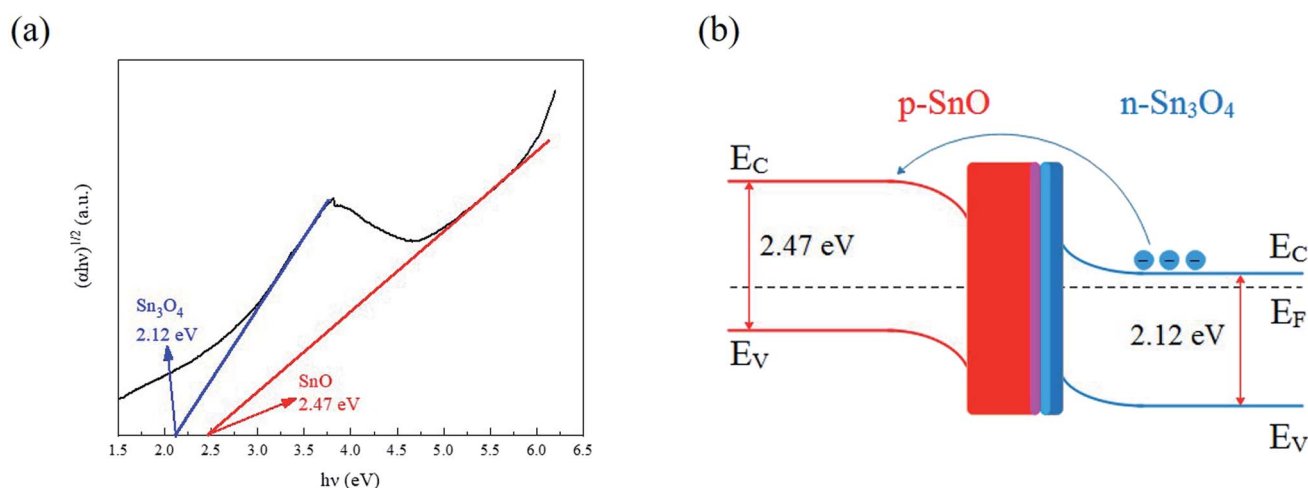

Fig. 12 (a) Plots of $(\alpha h\nu)^{1/2}$ against the photon energy ($h\nu$) for the SnO–Sn_3O_4 heterostructure. (b) Schematic of the energy structure of the SnO–Sn_3O_4 heterostructure.

4. Conclusion

The SnO–Sn$_3$O$_4$-heterostructure-based material was fabricated and used as an NO$_2$ sensor. The morphology, structure, and composition characterizations revealed its 3D flower-like microparticles structure assembled by 2D nanosheets, in situ-formed SnO–Sn$_3$O$_4$ heterostructure, and large specific surface area. The gas sensing measurements showed the excellent NO$_2$ sensing performance of the SnO–Sn$_3$O$_4$ heterostructure. Its responses were as high as 657.4 and 63.4 to 500 ppb of NO$_2$ while its limits of detection were as low as 2.5 and 10 ppb at 75 °C and ambient temperature, respectively. In addition, the SnO–Sn$_3$O$_4$ heterostructure exhibited an excellent selectively to NO$_2$, even if exposed to mixture gases containing interferential part with high concentration. The high performances were attributed to the in situ formation of SnO–Sn$_3$O$_4$ p–n hetero-junctions and large specific surface area. The SnO–Sn$_3$O$_4$ heterostructure having the excellent NO$_2$ sensing performance is promising for applications as an NO$_2$ sensor or alarm operated at a low operating temperature.

Conflicts of interest

There are no conflicts to declare.

Acknowledgements

References

1 H. Long, A. Harley-Trochimczyk, T. Pham, Z. Tang, T. Shi, A. Zettl, et al., High Surface area MoS$_2$/graphene hybrid aerogel for ultrasensitive NO$_2$ detection, Adv. Funct. Mater., 2016, 26, 5158–5165.

2 WHO Regional Office for Europe, Health aspects of air pollution with particulate matter, ozone and nitrogen dioxide: report on a WHO working group, Bonn, January 2003.

3 M. W. G. Hoffmann, J. D. Prades, L. Mayrhofer, F. Hernandez-Ramirez, T. T. Järvi, M. Moseler, A. Waag and H. Shen, Highly selective SAM–nanowire hybrid NO$_2$ sensor: insight into charge transfer dynamics and alignment of frontier molecular orbitals, Adv. Funct. Mater., 2014, 24, 595–602.

4 N. Barsan, D. Koziej and U. Weimar, Metal oxide-based gas sensor research: How to?, Sens. Actuators, B, 2007, 121, 18–35.

5 G. Li, X. Wang, L. Liu, R. Liu, F. Shen, Z. Cui, et al., Controllable Synthesis of 3D Ni(OH)$_2$ and NiO Nanowalls on Various Substrates for High-Performance Nanosensors, Small, 2015, 11, 731–739.

6 R. D. Bhusari, N. S. Ramgir, K. M. Avhad, R. Jishita, R. Navneethan, A. K. Debnath, et al., Development of NO$_2$ sensor based on Ti modified ZnO nanowires, International Conference on Sensing, 2017, pp. 229–233.

7 T. Kida, A. Nishiyama, M. Yuasa, K. Shimanoe and N. Yamazoe, Highly sensitive NO$_2$ sensors using lamellar-structured WO$_3$ particles prepared by an acidification method, Sens. Actuators, B, 2009, 135, 568–574.

8 D. Zhang, Z. Liu, C. Li, T. Tang, X. Liu, S. Han, et al., Detection of NO$_2$ Down to ppb Levels Using Individual and Multiple In$_2$O$_3$ Nanowire Devices, Nano Lett., 2012, 4, 1919–1924.

9 P. H. Suman, A. A. Felix, H. L. Tuller, J. A. Varela and M. O. Orlandi, Comparative gas sensor response of SnO$_2$, SnO and Sn$_3$O$_4$ nanobelts to NO$_2$ and potential interferents, Sens. Actuators, B, 2015, 208, 122–127.

10 J. Zhang, S. Wang, Y. Wang, Y. Wang, B. Zhu, H. Xia, et al., NO$_2$ sensing performance of SnO$_2$ hollow-sphere sensor, Sens. Actuators, B, 2009, 135, 610–617.

11 C. Gu, X. Xu, J. Huang, W. Wang, Y. Sun and J. Liu, Porous flower-like SnO$_2$ nanostructures as sensitive gas sensors for volatile organic compounds detection, Sens. Actuators, B, 2012, 174, 31–38.

12 S. Maeng, S. W. Kim, D. H. Lee, S. E. Moon, K. C. Kim and A. Maiti, SnO$_2$ nanoslab as NO$_2$ sensor: identification of the NO$_2$ sensing mechanism on a SnO$_2$ surface, ACS Appl. Mater. Interfaces, 2014, 6, 357–363.

13 Q. Wang, X. Kou, C. Liu, L. Zhao, T. Lin, F. Liu, et al., Hydrothermal synthesis of hierarchical CoO/SnO$_2$ nanostructures for ethanol gas sensor, J. Colloid Interface Sci., 2017, 513, 760–766.

14 Z. Zhang, M. Xu, L. Liu, X. Ruan, J. Yan, W. Zhao, et al., Novel SnO$_2$@ZnO hierarchical nanostructures for highly sensitive and selective NO$_2$ gas sensing, Sens. Actuators, B, 2018, 257, 714–727.

15 L. Xiao, S. Xu, G. Yu and S. Liu, Efficient hierarchical mixed Pd/SnO$_2$ porous architecture deposited microheater for low power ethanol gas sensor, Sens. Actuators, B, 2018, 255, 2002–2010.

16 R. Malik, V. K. Tomer, V. Chaudhary, M. S. Dahiya, S. P. Nehra, S. Duhan, et al., A low temperature, highly sensitive and fast response toluene gas sensor based on In(III)-SnO$_2$ loaded cubic mesoporous graphitic carbon nitride, Sens. Actuators, B, 2018, 255, 3564–3575.

17 J. Hao, D. Zhang, Q. Sun, S. Zheng, J. Sun and Y. Wang, Hierarchical SnS$_2$/SnO$_2$ nanoheterojunctions with increased active-sites and charge transfer for ultrasensitive NO$_2$ detection, Nanoscale, 2018, 10, 7210–7217.

18 M. A. Maki-Jaskari and T. T. Rantala, Possible structures of nonstoichiometric tin oxide: the composition Sn$_2$O$_3$, Modell. Simul. Mater. Sci. Eng., 2004, 12, 33–41.

19 F. Lawson, Tin Oxide—Sn$_3$O$_4$, Nature, 1967, 215, 955–956.

20 G. L. W. Hart, B. Volker, M. J. Walorski and Z. Alex, Evolutionary approach for determining first-principles hamiltonians, Nat. Mater., 2005, 4, 391–394.

21 P. H. Suman, E. Longo, J. A. Varela and M. O. Orlandi, Controlled synthesis of layered Sn$_3$O$_4$ nanobelts by carbothermal reduction method and their gas sensor properties, J. Nanosci. Nanotechnol., 2014, 14, 6662–6668.

22 X. Ma, J. Shen, D. Hu, L. Sun, Y. Chen, M. Liu, et al., Preparation of three-dimensional Ce-doped Sn_3O_4 hierarchical microsphere and its application on formaldehyde gas sensor, J. Alloys Compd., 2017, 726, 1092–1100.

23 P. H. Suman, A. A. Felix, H. L. Tuller, J. A. Varela and M. O. Orlandi, Giant chemo-resistance of SnO disk-like structures, Sens. Actuators, B, 2013, 186, 103–108.

24 J. Liu, C. Wang, Q. Yang, Y. Gao, X. Zhou, X. Liang, et al., Hydrothermal synthesis and gas-sensing properties of flower-like Sn_3O_4, Sens. Actuators, B, 2016, 224, 128–133.

25 D. R. Miller, S. A. Akbar and P. A. Morris, Nanoscale metal oxide-based heterojunctions for gas sensing: a review, Sens. Actuators, B, 2014, 204, 250–272.

26 H. J. Kim and J. H. Lee, Highly sensitive and selective gas sensors using p-type oxide semiconductors: overview, Sens. Actuators, B, 2014, 192, 607–627.

27 F. Ren, L. Gao, Y. Yuan, Y. Zhang, A. Alqrni, O. M. Al-Dossary, et al., Enhanced BTEX gas-sensing performance of CuO/SnO_2 composite, Sens. Actuators, B, 2016, 223, 914–920.

28 G. Cui, G. Liang, B. Yao, S. Wang, P. Zhang and M. Zhang, Electrochemistry of CuO/In_2O_3 p–n heterojunction nano/microstructure array with sensitivity to H_2 at and below room-temperature, Electrochem. Commun., 2013, 30, 42–45.

29 Q. Xu, D. Ju, Z. Zhang, S. Yuan, J. Zhang, H. Xu, et al., Near room-temperature triethylamine sensor constructed with CuO/ZnO P-N heterostructural nanorods directly on flat electrode, Sens. Actuators, B, 2016, 225, 16–23.

30 S. W. Choi, A. Katoch, J. H. Kim and S. S. Kim, Prominent reducing gas-sensing performances of n-SnO_2 nanowires by local creation of p–n heterojunctions by functionalization with p-Cr_2O_3 nanoparticles, ACS Appl. Mater. Interfaces, 2014, 6, 17723–17729.

31 H. Gao, L. Zhao, L. Wang, P. Sun, H. Lu, F. Liu, et al., Ultrasensitive and low detection limit of toluene gas sensor based on SnO_2-decorated NiO nanostructure, Sens. Actuators, B, 2018, 255, 3505–3515.

32 L. Li, C. Zhang and W. Chen, Fabrication of SnO_2-SnO nanocomposites with p–n heterojunctions for the low-temperature sensing of NO_2 gas, Nanoscale, 2015, 7, 12133–12142.

33 H. Yu, T. Yang, Z. Wang, Z. Li, Q. Zhao and M. Zhang, p–n heterostructural sensor with SnO-SnO_2 for fast NO_2 sensing response properties at room temperature, Sens. Actuators, B, 2018, 258, 517–526.

34 A. Shanmugasundaram, P. Basak, L. Satyanarayana and S. V. Manorama, Hierarchical SnO/SnO_2 nanocomposites: Formation of in situ p–n junctions and enhanced H_2 sensing, Sens. Actuators, B, 2013, 185, 265–273.

35 W. Zeng, Y. Liu, J. Mei, C. Tang, K. Luo, S. Li, et al., Hierarchical SnO_2–Sn_3O_4 heterostructural gas sensor with high sensitivity and selectivity to NO_2, Sens. Actuators, B, 2019, 127010.

36 L. Brewer, Thermodynamic Properties of the Oxides and Their Vaporization Processes, Chem. Rev., 1953, 52, 1–75.

37 Z. Dai, Z. Pan and Z. Wang, Growth and structure evolution of novel tin oxide diskettes, J. Am. Chem. Soc., 2002, 124, 8673–8680.

38 A. Seko, A. Togo, F. Oba and I. Tanaka, Structure and stability of a homologous series of tin oxides, Phys. Rev. Lett., 2008, 100, 045702.

39 J. H. Lee, Gas sensors using hierarchical and hollow oxide nanostructures: overview, Sens. Actuators, B, 2009, 140, 319–336.

40 T. Yang, J. Zhao, X. Li, X. Gao, C. Xue, Y. Wu, et al., Preparation and characterization of p-type transparent conducting SnO thin films, Mater. Lett., 2015, 139, 39–41.

41 W. Guo, L. Fu, Y. Zhang, K. Zhang, L. Liang, Z. Liu, et al., Microstructure, optical, and electrical properties of p-type SnO thin films, Appl. Phys. Lett., 2010, 96, 042113.

42 S. Park, S. An, Y. Mun and C. Lee, UV-enhanced NO_2 gas sensing properties of SnO_2-core/ZnO-shell nanowires at room temperature, ACS Appl. Mater. Interfaces, 2013, 5, 4285–4292.

43 B. Y. Yeh, P. F. Huang and W. J. Tseng, Enhanced room-temperature NO_2 gas sensing with TeO_2/SnO_2 brush- and bead-like nanowire hybrid structures, Nanotechnology, 2017, 28, 045501.

44 J. H. Cha, S. J. Choi, S. Yu and I. D. Kim, 2D WS_2-edge functionalized multi-channel carbon nanofibers: effect of WS_2 edge-abundant structure on room-temperature NO_2 sensing, J. Mater. Chem. A, 2017, 5, 8725–8732.

45 B. Zhang, G. Liu, M. Cheng, Y. Gao, L. Zhao, S. Li, et al., The preparation of reduced graphene oxide-encapsulated α-Fe_2O_3 hybrid and its outstanding NO_2 gas sensing properties at room temperature, Sens. Actuators, B, 2018, 261, 252–263.

46 F. Gu, R. Nie, D. Han and Z. Wang, In_2O_3–graphene nanocomposite based gas sensor for selective detection of NO_2 at room temperature, Sens. Actuators, B, 2015, 219, 94–99.

47 L. Guan, S. Wang, W. Gu, J. Zhuang, H. Jin, W. Zhang, et al., Ultrasensitive room-temperature detection of NO_2 with tellurium nanotube based chemiresistive sensor, Sens. Actuators, B, 2014, 196, 321–327.

48 S. Thirumalairajan, K. Girija, V. R. Mastelaro and N. Ponpandian, Surface morphology-dependent room-temperature $LaFeO_3$ nanostructure thin films as selective NO_2 gas sensor prepared by radio frequency magnetron sputtering, ACS Appl. Mater. Interfaces, 2014, 6, 13917–13927.

49 S. Mao, S. Cui, G. Lu, K. Yu, Z. Wen and J. Chen, Tuning gas-sensing properties of reduced graphene oxide using tin oxide nanocrystals, J. Mater. Chem., 2012, 22, 11009–11013.

50 N. Yamazoe, J. Fuchigami, M. Kishikawa and T. Seiyama, Interactions of tin oxide surface with O_2, H_2O and H_2, Surf. Sci., 1979, 86, 335–344.

51 L. I. Trakhtenberg, G. N. Gerasimov, V. F. Gromov, T. V. Belysheva and O. J. Ilegbusi, Effect of composition on sensing properties of SnO_2+In_2O_3 mixed nanostructured films, Sens. Actuators, B, 2012, 169, 32–38.

52 X. Xu, P. Zhao, D. Wang, P. Sun, L. You, Y. Sun, et al., Preparation and gas sensing properties of hierarchical

flower-like In_2O_3 microspheres, *Sens. Actuators, B*, 2013, **176**, 405–412.

53 J. Zhang, R. Tan, Y. Yang, W. Xu, J. Li, W. Shen, *et al.*, Synthesis mechanism of heterovalent Sn_2O_3 nanosheets in oxidation annealing process, *Chin. Phys. B*, 2015, **24**, 178–182.

54 L. Wang, D. Wang, Z. Dong, F. Zhang and J. Jin, Interface chemistry engineering of protein-directed SnO_2 nanocrystal-based anode for lithium-ion batteries with improved performance, *Small*, 2014, **10**, 998–1007.

55 T. Yoshida, N. Ogawa and T. Takahashi, Influence of NO and NO_2 composition on resistivity changes of SnO_2, *J. Electrochem. Soc.*, 1999, **146**(3), 1106–1110.

56 S. Elzey, A. Mubayi, S. C. Larsen and V. H. Grassian, FTIR study of the selective catalytic reduction of NO_2 with ammonia on nanocrystalline NaY and CuY, *J. Mol. Catal. A: Chem.*, 2008, **285**(1–2), 48–57.

57 H. Zhang, L. Yu, Q. Li, Y. Du and S. Ruan, Reduced graphene oxide/α-Fe_2O_3 hybrid nanocomposites for room temperature NO_2 sensing, *Sens. Actuators, B*, 2017, **241**, 109–115.

58 H. Hosono, Y. Ogo, H. Yanagi and T. Kamiya, Bipolar conduction in SnO thin films, *Electrochem. Solid-State Lett.*, 2011, **14**, H13–H16.

59 W. Xia, H. Qian, X. Zeng, J. Dong, J. Wang and Q. Xu, Visible-light self-powered photodetector and recoverable photocatalyst fabricated from vertically aligned Sn_3O_4 nanoflakes on carbon paper, *J. Phys. Chem. C*, 2017, **121**, 19036–19043.

60 H. Zhang, J. Feng, T. Fei, S. Liu and T. Zhang, SnO_2 nanoparticles-reduced graphene oxide nanocomposites for NO_2 sensing at low operating temperature, *Sens. Actuators, B*, 2014, **190**, 472–478.